Article:
Jiang, G., Zhou, H., Ye, C. et al. (2025) Comparative analysis of hybrid dual permanent magnet machines with different asymmetric stator-pole topologies. Journal of Electrical Engineering & Technology, 20 (7). pp. 4627-4642. ISSN: 1975-0102

https://doi.org/10.1007/s42835-025-02300-8

Comparative Analysis of Hybrid Dual Permanent Magnet Machines with Different Asymmetric Stator-Pole Topologies

Guangyao Jiang *, Huawei Zhou†, Chen Ye**, Guang-Jin Li*** and Yu Zeng****

Abstract - This paper presents a hybrid dual permanent magnet (HDPM) machine that combines stator-mounted NdFeB magnets with rotor-embedded ferrites in a consequent-pole configuration, enhancing permanent magnet utilization while reducing rare-earth material consumption. The proposed design leverages a bidirectional modulation effect and an asymmetric stator-pole (ASP) topology to generate high-torque working harmonics. Four HDPM variants with Halbach-array ferrite rotors and distinct ASP structures are optimized using a multi-objective non-dominated sorting genetic algorithm II (NSGA-II), and their electromagnetic performance is comparatively analyzed. The results reveal superior torque density and efficiency in the proposed machine. Additionally, a 3D finite element analysis investigates the torque-enhancement mechanism of the rotor-ferrite overhang structure. Finally, experimental validation via a fabricated split stator-pole HDPM-ASP prototype confirms the machine's effectiveness.

Keywords: Asymmetric stator pole, Bidirectional flux modulation effect, Consequent pole, Hybrid dual permanent magnet machines.

1. Introduction

Growing environmental concerns and fossil fuel shortages have accelerated the development of electric machines for zero-emission vehicles [1]-[2]. Among various propulsion technologies, permanent magnet (PM) machines employing NdFeB magnets have become a primary research focus due to their outstanding torque density and efficiency [3]-[4]. However, both stator-PM and rotor-PM machines suffer from inherent limitations of single-sided excitation, which fundamentally restricts their torque capability [5]-[8]. In contrast, dual permanent magnet (DPM) machines, featuring PMs in both stator and rotor, leverage bidirectional flux modulation to enhance working harmonics, emerging as a promising solution for superior torque density [9]-[13].

DPM machines achieve bidirectional flux modulation through the synergistic interaction of dual PMs and dual flux modulators (stator and rotor salient poles), which collectively enhance magnetic field harmonics [9]. In [10], a DPM machine utilizing this effect was proposed and demonstrated its torque advantages through comparative analysis with conventional stator-PM machine and rotor-PM machine. This study revealed that the torque density of the DPM machine is 63% higher than that of the stator-PM machine and 25% higher than that of the rotor-PM machine under similar PM material volumes. However, these structures exhibit larger leakage flux, resulting in a lower PM utilization ratio. To increase PM utilization, the PMs based on the Halbach array were usually embedded in the stator part [11]-[12] and rotor part [13] of DPM machines to enhance local flux density through flux-concentrating effect. Nonetheless, the aforementioned designs required additional PMs to maintain sinusoidal distribution of flux density, resulting in high manufacturing cost that remains a critical challenge.

Recent efforts to address cost challenges have explored three key approaches: consequent-pole (CP) arrangements [14]-[16], asymmetric stator pole (ASP) configurations [17], and hybrid magnetic pole designs [18]-[19]. CP topologies reduce cost through alternately mounted magnets, ASP topologies reduce cost through generating additional harmonic components to balance torque, while hybrid magnetic pole topologies leverage synergy between high-performance rare-earth magnets and low-cost ferrite magnets. In [20], a DPM machine with complementary CP arrangement and ASP configuration was proposed, which alternately mounted the PMs on the stator teeth. Its results demonstrated that the machine could provide better electromagnetic performance due to reduced leakage flux, but torque enhancement was limited by the stator tooth width. Although achieving sector-specific gains in both torque and production costs, these developments maintain their requirement for NdFeB magnets in the rotor configuration. While hybrid magnetic pole designs that combine rare-earth and ferrite magnets reduce costs through series/parallel rotor configurations [18]-[19], their

† Corresponding Author : School of Electrical and Information Engineering, Jiangsu University, Zhenjiang 212013, China. (zhouhuawei@ujs.edu.cn)

* School of Electrical and Information Engineering, Jiangsu University, Zhenjiang 212013, China. (2112207008@stmail.ujs.edu.cn)

** School of Electrical and Information Engineering, Jiangsu University, Zhenjiang 212013, China. (2112307112@stmail.ujs.edu.cn)

*** Dept. of Electronic and Electrical Engineering, The University of Sheffield, S1 3JD Sheffield, U.K.. (g.li@sheffield.ac.uk)

**** School of Electrical and Information Engineering, Jiangsu University, Zhenjiang 212013, China. (zengyu@ujs.edu.cn)

Received 23 Nov 2024 ; Accepted 13 May 2025

performance remains constrained by single-sided excitation. Thus, integrating the hybrid magnetic pole topology with the ASP-based DPM machine by partially replacing rare-earth magnets with cost-effective ferrites, provides an optimal compromise between performance and cost.

The objective of this paper is to propose a novel hybrid dual permanent magnet (HDPM) machine combining asymmetric stator-pole (ASP) topologies and a Halbach-array-based hybrid magnetic pole design. The proposed machine achieves superior torque density and PM utilization while drastically reducing rare-earth magnet usage. A comprehensive analysis of the magnetic field characteristics, particularly the stator pole distribution's influence on air-gap working harmonics, is presented. Multi-objective optimization further demonstrates the machine's electromagnetic performance advantages. The main novelties and contributions are summarized as follows.

(1) The hybrid magnetic pole design was applied to the DPM machine topology, resulting in a HDPM machine with an asymmetric stator pole. This design consists of stator NdFeB magnets and rotor ferrites, combined with CP array, which effectively reduces the use of rare-earth materials, thereby lowering material costs while maintaining high torque performance. Additionally, the rotor ferrite with Halbach array was employed to further improve PM utilization and enhance torque.

(2) Using the magnetomotive force (MMF) permeance model, the air-gap flux density of four HDPM machines with different ASP topologies was analyzed. This helps establish the relationship between the stator magnetic pole distributions and the resulting working harmonic orders. It was revealed that the major working harmonic orders were altered by the different stator magnetic pole distributions, even when using the same slot-pole combination.

(3) The impact of the rotor-ferrite overhang structure on torque enhancement was investigated, including an analysis of how the overhang length influences torque performance.

2. Topology and Operation Principle

To reduce rare-earth material usage and improve torque density, the stator topologies with different permanent magnet arrangements are presented and combined with a Halbach array rotor to form four distinct DPM machines. Additionally, their operating principles are analyzed.

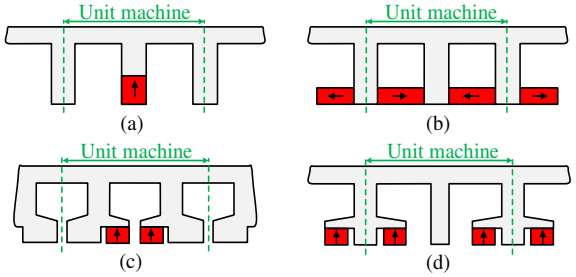

Fig. 1. Topologies of (a) stator tooth, (b) stator slot, (c) stator pole and (d) split stator pole.

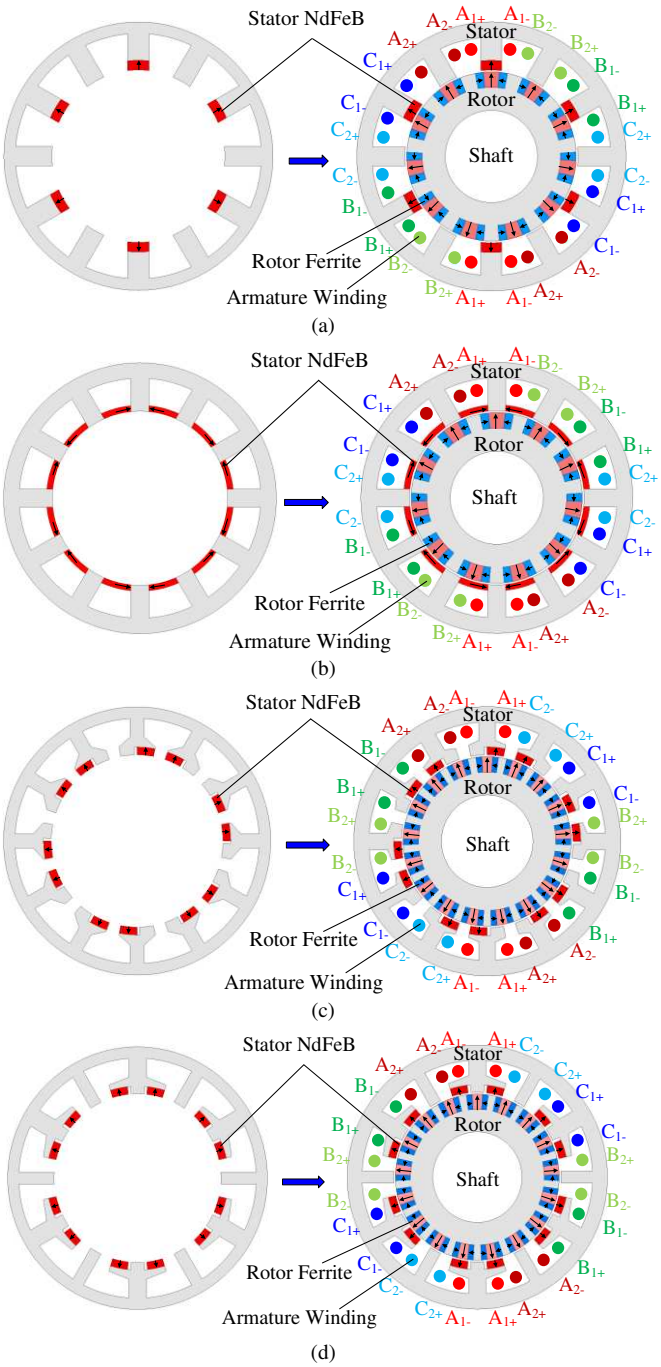

Fig. 2. Topologies of (a) M1, (b) M2, (c) M3 and (d) M4.

Table 1. Design specification of four machines

Items	M1	M2	M3	M4
Number of stator slots	12			
Stator pole pairs	6		12	
Rotor pole pairs	11		17	
Stator outer diameter (mm)	140			
Stator inner diameter (mm)	90			
Rotor outer diameter (mm)	88			
Rotor inner diameter (mm)	50			
Number of turns per phase	50			
Rated speed (r/min)	300			
Active length (mm)	50			
Current density (A/mm^2)	5			
NdFeB material	N35SH			
Ferrite material	FB12H			
Iron core material	DW540-50			

2.1 Machine Topologies

The hybrid magnetic pole design with a bidirectional flux modulation effect was employed in designing HDPM machines. Depending on the positions of the NdFeB magnet and iron in the stator, the ASP topologies can be primarily categorized into four types: (a) stator tooth, (b) stator slot, (c) stator pole, and (d) split stator pole, as shown in Fig. 1. With the same CP rotor employing Halbach-array ferrites, these different ASP topologies can lead to four typical HDPM machines: stator-tooth HDPM machine (called M1), stator-slot HDPM machine (called M2), stator-pole HDPM machine (called M3), and proposed split stator-pole HDPM machine (called M4), as shown in Fig. 2. The flux-concentrating direction of rotor ferrites is both oriented radially outward. Fig. 2(a) shows the topology of M1 as reported in [18]. The magnetic and iron poles are alternately arranged on the stator teeth to create a CP array, and all NdFeB magnets are parallelly outward magnetized. Thus, combined with the rotor ferrites, it can achieve a bidirectional flux modulation effect. Fig. 2(b) shows the topology of M2 [18]. The NdFeB magnets are placed in the stator slots, and the adjacent magnets are tangentially magnetized with opposite magnetizing directions. The stator teeth and the adjacent NdFeB magnets form the CP array. Then, the stator teeth can be employed as modulators to modulate air gap flux. To weaken the leakage flux present in the stator of M2, M3 with auxiliary slots and NdFeB magnets on the stator teeth was proposed [17], as shown in Fig. 2(c). The NdFeB magnets with radially outward magnetization are embedded in stator teeth, and they form the CP array with the adjacent stator teeth.

To further enhance the torque density, M4 with a special ASP design shown in Fig. 1(d) was proposed in this paper, as shown in Fig. 2(d). The ASP design features asymmetric magnet configuration, i.e., "Magnet-Iron-Magnet tooth, Iron tooth, Magnet-Iron-Magnet tooth, ...". This combines with CP rotor ferrites to enrich the working harmonics. Furthermore, the auxiliary slots are set in the stator to further weaken the leakage flux. The corresponding design specifications of these machines are listed in Table 1.

2.2 Operating Principle

Similar to the existing DPM machines [18], the operating principle of the four machines is based on the bidirectional flux modulation effect, i.e., the magnetic fields generated by the stator NdFeB magnets and rotor ferrites are modulated by the stator and rotor teeth. To illustrate the operating principle and the difference between the four machines, the simplified MMF and permeance distributions of the four machines are shown in Fig. 3. The stator MMF considering the stator permeance and the rotor MMF considering the rotor permeance can be expressed as

$$\begin{cases} F_S(\theta) = \sum_{m=1}^{\infty} F_{Sm} \cos(\frac{mP_s}{p}\theta) \\ F_R(\theta,t) = \sum_{i=1}^{\infty} F_{Ri} \cos[iP_r(\theta - \omega_r t)] \end{cases} \quad (1)$$

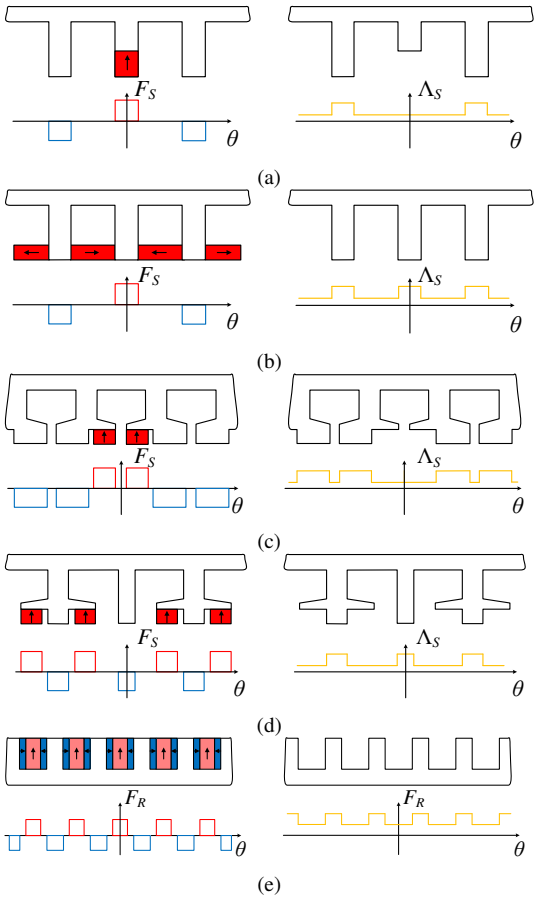

Fig. 3. Stator MMF and permeance distributions of (a) M1, (b) M2, (c) M3 and (d) M4, and (e) rotor MMF and permeance distributions.

where F_{sm} and F_{ri} are the amplitudes of stator NdFeB magnet and rotor ferrite excited MMF Fourier series, respectively; m and i are the order of the Fourier series, respectively; P_s, and P_r are the pole-pair numbers of stator NdFeB magnet and rotor ferrite, respectively; p is the pole-pair numbers of stator NdFeB magnet in a unit machine; θ and ω_r are the mechanical position in stationary coordinate and rotating speed of rotor, respectively.

The stator permeance and rotor permeance can be respectively expressed as

$$\begin{cases} \Lambda_S(\theta) = \Lambda_{S0} + \sum_{j=1}^{\infty} \Lambda_{Sj} \cos(\frac{jN_s}{s}\theta) \\ \Lambda_R(\theta,t) = \Lambda_{R0} + \sum_{n=1}^{\infty} \Lambda_{Rn} \cos[nN_r(\theta - \omega_r t)] \end{cases} \quad (2)$$

where Λ_{S0}, Λ_{Sj}, Λ_{R0}, and Λ_{Rn} are the Fourier series coefficients of stator and rotor, respectively; j and n are the order of Fourier series, respectively; N_s and N_r are the slot numbers of stator and rotor, respectively; s is the symmetric slots in a unit machine.

Consequently, the air-gap flux density excited by stator NdFeB magnets and rotor ferrites can be obtained as

$$
\begin{aligned}
B_g(\theta,t) &= B_{Sg}(\theta,t) + B_{Rg}(\theta,t) \\
&= F_S(\theta)\Lambda_R(\theta,t) + F_R(\theta,t)\Lambda_S(\theta) \\
&= \Lambda_{R0}\sum_{m=1}^{\infty} F_{Sm}\cos(\frac{mP_s}{p}\theta) \\
&+ \sum_{m=1}^{\infty}\sum_{n=1}^{\infty}\frac{F_{Sm}\Lambda_{Rn}}{2}\cos\left[(\frac{mP_s}{p}\pm nN_r)\theta \mp nN_r\omega_r t\right] \\
&+ \Lambda_{S0}\sum_{i=1}^{\infty} F_{Ri}\cos[iP_r(\theta-\omega_r t)] \\
&+ \sum_{i=1}^{\infty}\sum_{j=1}^{\infty}\frac{F_{Ri}\Lambda_{Sj}}{2}\cos\left[(iP_r\pm\frac{jN_s}{s})\theta - iP_r\omega_r t\right]
\end{aligned} \tag{3}
$$

It is worth noting that the pole-pair numbers of the stator MMF and permeance can change due to the asymmetric design, which will generate additional harmonics during the flux modulation process. Furthermore, the magnetic fields excited by stator NdFeB magnets and rotor ferrites interact with the magnetic field excited by the armature windings to obtain steady torque performance, i.e., the pole-pair numbers and rotating speeds of magnetic fields excited by armature winding need to be equal to that excited by stator NdFeB magnets and rotor ferrites, which means

$$
\begin{cases}
kP_a = \left|mP_s / p \pm nN_r\right|; \quad \omega_a = \dfrac{\mp nN_r}{mP_s / p \pm nN_r}\omega_r \\
kP_a = \left|iP_r \pm jN_s / s\right|; \quad \omega_a = \dfrac{-iP_r}{iP_r \pm jN_s / s}\omega_r \\
k = 1,3,5...; \; m,i = 1,2,3...; \; n,j = 0,\pm1,\pm2...
\end{cases} \tag{4}
$$

where P_a is the pole-pair numbers of armature winding; ω_a is the rotating speed of armature field; p/s is 1/2, 1/1, 2/2, and 2/2 for M1, M2, M3, and M4, respectively, i.e., the working harmonics are $|mP_s \pm nN_r|$ and $|iP_r \pm jN_s/2|$ for M1, $|mP_s \pm nN_r|$ and $|iP_r \pm jN_s|$ for M2, and $|mP_s/2 \pm nN_r|$ and $|iP_r \pm jN_s/2|$ for M3 and M4.

3. Optimization Design

To obtain better electromagnetic performance, the key design parameters of these machines shown in Fig. 4 are optimized using a non-dominated sorting genetic algorithm II (NSGA-II) [21]-[22]. This optimization aims to achieve maximum average torque, minimum torque ripple, and highest efficiency with the algorithm's parameters such as the population number, maximum iteration generation, crossover factor, and mutator factor being set as 200, 50, 0.8, and 0.4, respectively. Meanwhile, the optimization ranges of the variables for these machines are listed in Table 2.

During the optimization process, the stator outer diameter, air-gap length, active stack length, and copper loss remain constant. Furthermore, the optimization functions and constraints are as follows.

$$
\begin{aligned}
&\text{Objective}: \left\{\max(f_T), \min(f_R), \max(f_E)\right\} \\
&\text{Constraints}: \begin{cases}
\min x_i \le x_i \le \max x_i \\
\text{M1}: f_T \ge 5, f_R \ge 10, f_E \ge 76 \\
\text{M2}: f_T \ge 4, f_R \ge 10, f_E \ge 70 \\
\text{M3}: f_T \ge 8, f_R \ge 10, f_E \ge 80 \\
\text{M4}: f_T \ge 9, f_R \ge 10, f_E \ge 85
\end{cases}
\end{aligned} \tag{5}
$$

where x_i is the design parameter variables; min and max are the maximum and minimum values of x_i, respectively; f_T, f_R, and f_E are the optimized values of average torque, torque ripple, and efficiency, respectively. In addition, f_T and f_R can be directly obtained by the FEM simulation. Only copper loss, iron loss, and PM eddy current loss are considered in the calculation of f_E.

Fig. 5 shows the Pareto front obtained by NSGA-II for M1, M2, M3, and M4. When the torque ripple is less than 10%, the machine with the highest torque and efficiency is selected as the optimal design, which is marked by the pink circle. The optimized design parameters and optimization results of the four machines are listed in Tables 3 and 4, respectively. It can be noted that the torque of the four machines is increased while reducing the torque ripple and improving the efficiency, where the torque of M1, M2, M3, and M4 is increased by 20%, 9.3%, 12.2%, and 18.5%, respectively.

Table 2. Optimization range of design parameters

Parameters	Range			
	M1	M2	M3	M4
T_{sy} (mm)	4-8	4-8	4-8	4-8
T_{st1} (mm)	6.7-11	4.4-11	6.7-11	6.7-11
T_{st2} (mm)	4.4-9	-	-	4.4-9
H_{st} (mm)	-	-	1-4	1-4
H_{sp} (mm)	3-10	3-5	3-5	3-5
W_{sp} (°)	-	-	9-15	9-15
W_{st} (°)	-	-	6-14	6-14
W_{sa} (°)	-	-	1-4	1-4
W_{rf1} (°)	8.2-11.4	8.2-11.4	5.4-7.4	5.4-7.4
W_{rf2} (°)	4.1-5.7	4.1-5.7	2.7-3.7	2.7-3.7

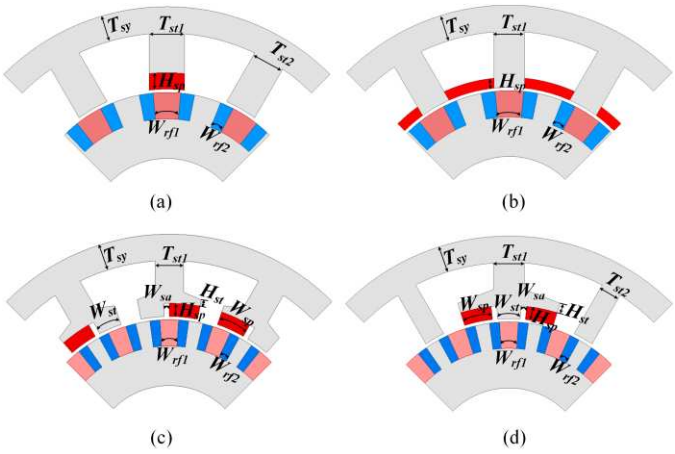

Fig. 4. Parameter models of (a) M1, (b) M2, (c) M3 and (d) M4.

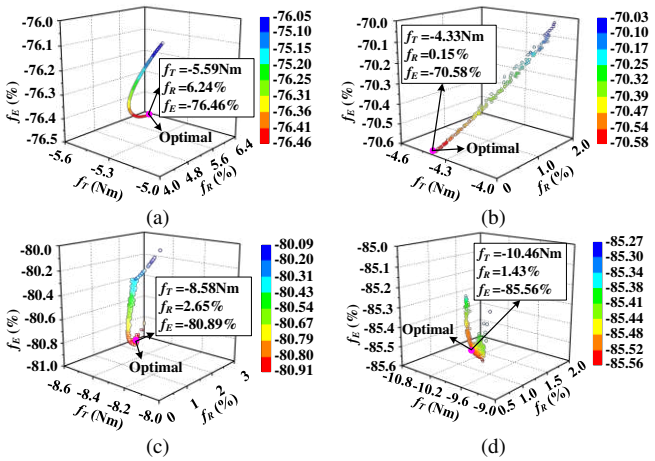

Fig. 5. Pareto front of NSGA-II. (a) M1. (b) M2. (c) M3. (d) M4.

Table 3. Optimized design parameters of four machines

Items	M1	M2	M3	M4
Stator outer diameter (mm)		140		
Stator inner diameter (mm)		90		
Air-gap length (mm)		1		
Rated current (A)		7.07		
Rated current density (A/mm^2)		5		
Number of turns per phase		50		
Active length L_{stack} (mm)		50		
Stator yoke thickness T_{sy} (mm)	7.8	7.5	5.8	6
Stator teeth width T_{st1}/T_{st2}	10.8/9.8	9.3	7.4	9.6/6.5
Stator side tooth heigh H_{st} (mm)	-	-	1.1	3
Stator NdFeB height H_{sp} (mm)	5	3	4	4
Stator NdFeB width W_{sp} (°)	-	-	11	11
Stator tooth-tip width W_{st} (°)	-	-	9.25	8.7
Auxiliary slot width W_{sa} (°)	-	-	1.75	2
Rotor ferrite width W_{rf1}/W_{rf2}	11/5.5	11.2/5.6	7.3/3.7	7.3/4

Table 4. Optimization results of four machines

		M1	M2	M3	M4
f_T (Nm)	Initial value	4.66	3.96	7.65	8.83
	Optimal value	5.59	4.33	8.58	10.46
f_R (%)	Initial value	12.91	4.78	8.29	8.3
	Optimal value	6.24	0.15	2.65	1.43
f_E (%)	Initial value	75.49	69.41	79.43	84.64
	Optimal value	76.46	70.58	80.89	85.56

4. Comparative Study

To confirm the superiority of the proposed machine (M4), its electromagnetic characteristics were investigated and compared with those of three other machines. To ensure a fair comparison, all four machines were subjected to the same constraints, including stator outer diameter, stack length, copper loss, and zero *d*-axis current control strategy. Additionally, to obtain the maximum average torque, the four machines were designed with appropriate slot-pole combinations and further optimized using NSGA-II.

4.1 Comparison of Open-Circuit Performance

The electromagnetic performance comparison among the four machines was studied using FEM. The studied open-circuit performances include flux distribution, air-gap field distribution, and back-EMF. The flux distribution under open-circuit condition is shown in Fig. 6. It can be noticed that M2 has more leakage flux between stator poles when compared with M1, which will result in M2 losing more torque. Meanwhile, compared to M4, the flux lines in M3 span multiple stator slot pitches, which would result in increased iron loss in M3. In addition, there is slight magnetic saturation in the stator and rotor teeth tips of all four machines.

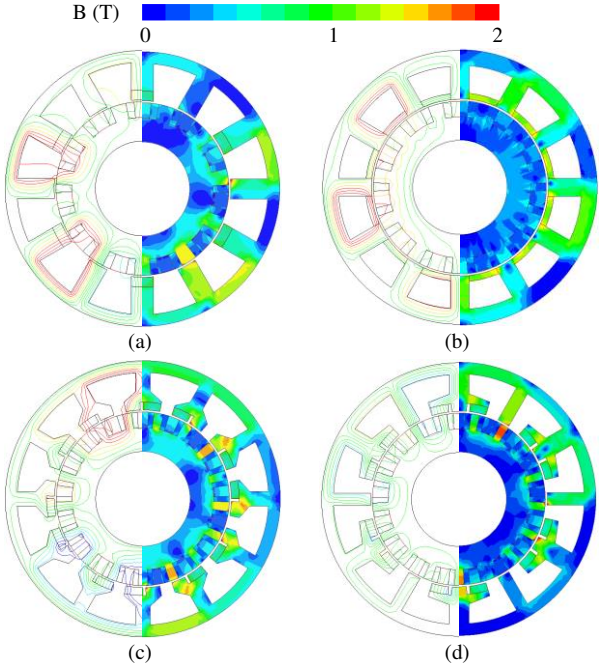

Fig. 6. Open-circuit flux distribution of (a) M1, (b) M2, (c) M3 and (d) M4.

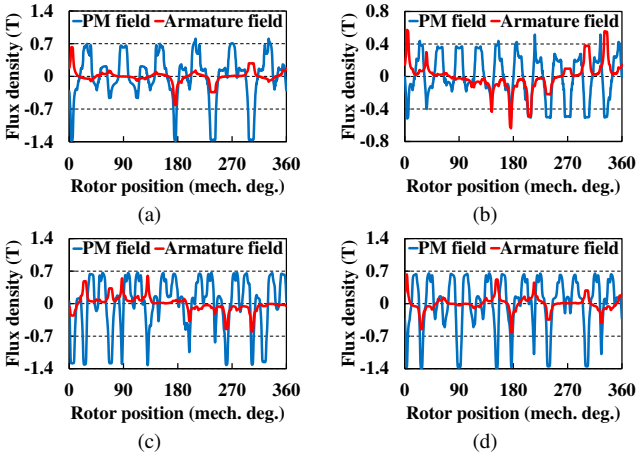

Fig. 7. Open-circuit air-gap field distribution of (a) M1, (b) M2, (c) M3 and (d) M4.

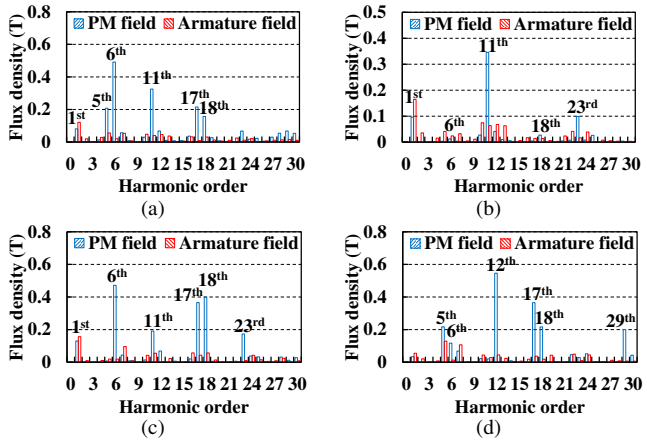

Fig. 8. Open-circuit air-gap field harmonics of (a) M1, (b) M2, (c) M3 and (d) M4.

Table 5. Air-gap flux density harmonics of four machines

	M1	M2	M3	M4
Stator-NdFeB field	mP_s $\lvert mP_s \pm nN_r \rvert$	mP_s $\lvert mP_s \pm nN_r \rvert$	$mP_s/2$ $\lvert mP_s/2 \pm nN_r \rvert$	$mP_s/2$ $\lvert mP_s/2 \pm nN_r \rvert$
Rotor-ferrite field	iP_r $\lvert iP_r \pm jN_s/2 \rvert$	iP_r $\lvert iP_r \pm jN_s \rvert$	iP_r $\lvert iP_r \pm jN_s/2 \rvert$	iP_r $\lvert iP_r \pm jN_s/2 \rvert$

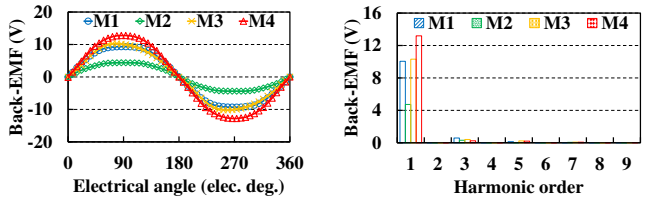

Fig. 9. Open-circuit phase back-EMF. (a) Waveforms. (b) Spectra.

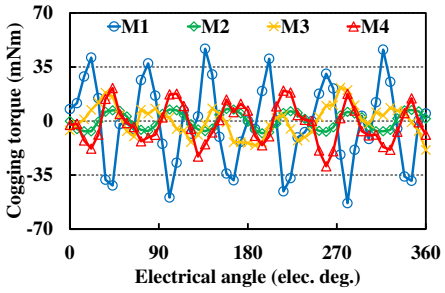

Fig. 10. Cogging torque.

The air-gap flux density and corresponding field harmonic components are shown in Figs. 7 and 8, respectively. It can be observed that besides the specific field harmonics excited by the stator-NdFeB, rotor-ferrite and armature currents in the four machines, many other major harmonics are generated due to the bidirectional flux modulation effect enabled by the uneven permeance distribution of the stator and rotor. These harmonics are 5th- and 17th-order harmonics for M1, 23rd-order harmonics for M2, 11th- and 23rd-order harmonics for M3, and 29th-order harmonics for M4. The comparison of Fig. 8(c) and Fig. 8(d) reveals that the major working harmonic contents are adjusted by the different stator magnetic pole distributions even with the same slot-pole combination. The above working harmonics agree well with the flux density harmonics listed in Table 5 and (1). The waveforms of open-circuit phase back-EMF at the rated speed of 300 r/min and corresponding harmonic components are shown in Fig. 9. It can be noticed that the amplitude of the fundamental back-EMF of the four machines is 10.1 V, 4.7 V, 10.3 V, and 13.2 V, respectively. Their total harmonic distortion (THD) of back-EMFs is 6%, 6.7%, 4.7%, and 2.5%, respectively, and the back-EMF amplitude of M4 is the largest. Fig. 10 shows the cogging torque waveform of the four machines. The peak-to-peak values of the cogging torque are 100.03, 15.73, 40.48, and 50.69 mNm, respectively. It can be noticed that M1 has the highest cogging torque and M2 with a slotless structure has the lowest cogging torque.

4.2 Comparison of On-Load Performance

The on-load performances of four machines under constant copper loss (P_c = 51 W) and zero d-axis current (I_d = 0 A) control are investigated. Based on the analysis of air-gap flux density harmonics, the contribution of the harmonics to torque is further studied by adopting the Maxwell stress tensor method [15]. Fig. 11 shows the contribution of air-gap flux density harmonics to torque in these machines. It can be observed that 5th-, 6th-, 11th-, 17th-, and 18th-order harmonics produce positive torque components for M1; 11th- and 23rd-order harmonics produce positive torque components for M2; 6th-, 11th-, 17th-, 18th-, and 23rd-order harmonics produce positive torque components for M3; 5th-, 12th-, 17th-, 18th-, and 29th-order harmonics produce positive torque components for M4. Furthermore, the contribution of these working harmonics to torque of the four machines is quantified, as listed in Table 6. It should be noted that the harmonic components corresponding to the rotor pole pairs in these machines are responsible for a major proportion of total torque, especially for M2. The contributions of harmonics generated by the ASP design to the torque of the four machines are 79.08%, 0.11%, 67.68%, and 9.33%, respectively. This indicates that the ASP design has a greater impact on M1, M3, and M4.

Since the difference in stator NdFeB magnet and rotor ferrite materials results in torque per PM volume not being a good representation of torque performance, the torque performance is compared by torque per PM cost (T/PMC). Fig. 12 shows the comparison diagram of the torque characteristics of these machines. It can be noticed from Fig. 12(a) that M4 has the highest torque while M2 with a larger leakage flux has the lowest torque. Meanwhile, the torque ripple of these machines shown in Fig. 12(a) is 2.49%, 2.01%, 5.48%, and 1.26%, which is inconsistent with the torque ripple in Table 4 due to the error between the FEM and optimization algorithm. Fig. 12(b) shows that M2 has the lowest T/PMC ratio, and M4 has a 48.94%, 204.35%, and 22.81% higher T/PMC ratio when compared with M1, M2, and M3, respectively. Fig. 12(c) shows the diagram of average torque versus current angle. Although zero torque is not at the current angle being equal to 90° due to the existence of reluctance torque generated by salient pole structure, the maximum average torques always occur at the

current angle being close to 0°, implying the negligible reluctance torque, which validates the selection of the $I_d = 0$ A control strategy. The relationships between average torque and q-axis peak current are shown in Fig. 12(d). It can be observed that M4 exhibits the highest average torque when the q-axis peak current is lower than 20 A. To evaluate the overloading capability, the coefficient k_{oc} is defined as

$$k_{oc} = \frac{f_{T20}}{f_{T10}} \tag{6}$$

where f_{T10} and f_{T20} are the torque under the q-axis peak current of 10 A and 20 A, respectively. The coefficient k_{oc} for M1, M2, M3, and M4 are calculated as: 1.84, 1.64, 1.48, and 1.69, respectively. It can be noticed that M1 exhibits the best overloading capability, while M4 is better than M2 and M3. It should be noted that M3 is more likely to suffer magnetic saturation when a large current is applied, thus reducing its torque capacity.

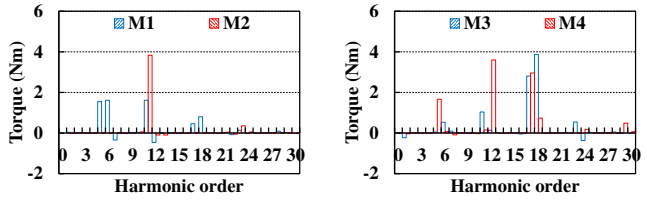

Fig. 11. Contribution of air-gap flux density harmonics to torque. (a) M1 and M2. (b) M3 and M4.

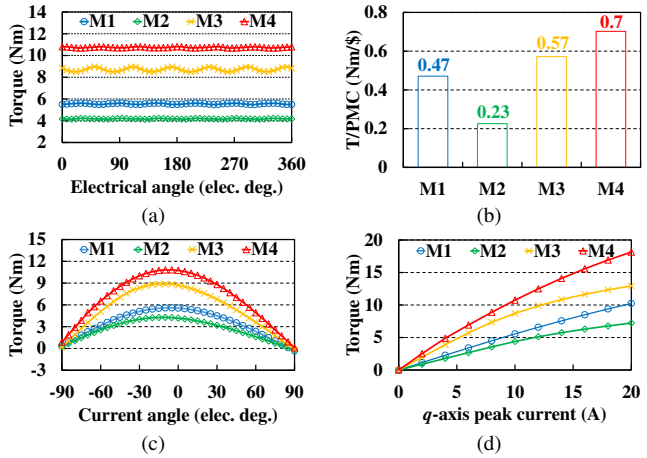

Fig. 12. Torque characteristics. (a) Torque. (b) T/PMC. (c) Torque versus current angle. (d) Torque versus q-axis peak current.

Table 6. Percentage of contribution from major working harmonics to torque

Order	M1	M2	M3	M4
5	27.69	-0.017	0.54	16.45
6	28.88	-0.028	6.02	0.8
11	28.93	93.69	11.72	1.49
12	-8.27	-2.4	1.53	35.63
17	8.23	0.0083	31.75	29.27
18	14.28	0.15	43.81	7.27
23	2.36	8.68	6.13	-0.23
29	0.45	-0.052	-0.048	4.83

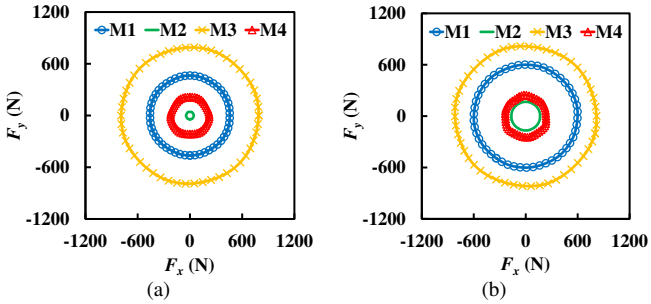

Fig. 13. UMF. (a) Open-circuit condition. (b) On-load condition.

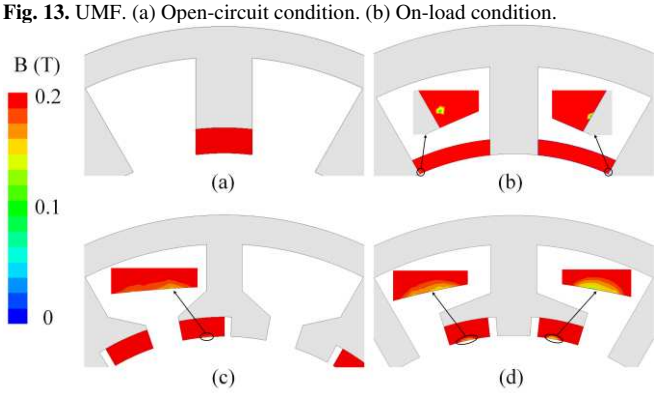

Fig. 14. Flux density of stator NdFeB magnets under d-axis demagnetization current. (a) M1. (b) M2. (c) M3. (d) M4.

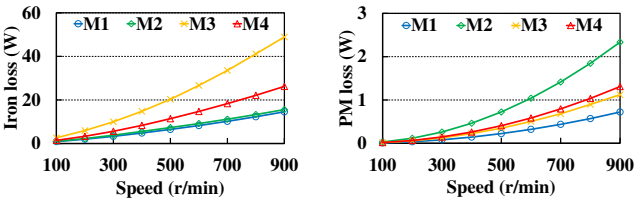

Fig. 15. Loss characteristics. (a) Iron loss. (b) PM loss.

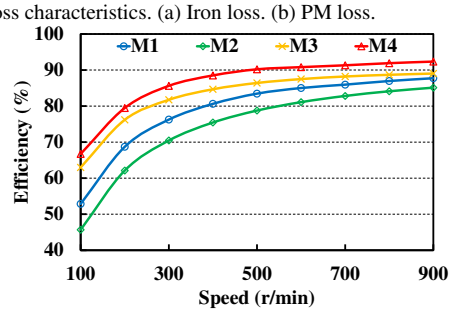

Fig. 16. Efficiency versus speed curves at rated current.

4.3 Unbalanced Magnetic Force Analysis

The unbalanced magnetic force (UMF) acting on the stator is caused by the asymmetric distribution in the air-gap flux density, which introduces additional vibration and noise and cannot be neglected. Therefore, the UMF distribution needs to be compared for the four machines. The force components in x- and y-axis such as F_x and F_y can be calculated by the Maxwell stress tensor method [23]

$$\begin{cases} F_x = \dfrac{rL_{stack}}{2\mu_0}\displaystyle\int_0^{2\pi}[(B_\theta^2 - B_r^2)\cos\theta + 2B_rB_\theta\sin\theta]d\theta \\ F_y = \dfrac{rL_{stack}}{2\mu_0}\displaystyle\int_0^{2\pi}[(B_\theta^2 - B_r^2)\sin\theta - 2B_rB_\theta\cos\theta]d\theta \end{cases} \tag{7}$$

where B_θ and B_r are the tangential and radial air-gap flux density components, respectively.

Fig. 13 shows the UMF distribution of the four machines under open-circuit and on-load conditions. It is worth noting that due to the odd number of rotor pole pairs, the four machines are inevitably affected by the UMF. M3 is the most affected by the UMF, and M2 is the least affected. Meanwhile, the UMF of the four machines is increased under on-load condition because of the asymmetric distribution of the armature reaction magnetic field, while M4 suffers the least.

4.4 Demagnetization Analysis

The ferrites are less prone to demagnetization with increasing temperature, so only the stator NdFeB magnets need to be analyzed for demagnetization. The anti-demagnetization capability of the stator NdFeB magnets for the four machines is investigated under a *d*-axis demagnetization current equal to 2.5 times rated current at 120 ℃, where the knee point of N35SH is 0.2 T [24]. Fig. 14 shows the stator-NdFeB flux density distribution of the four machines under this condition. It can be observed that except for M1, when M2, M3, and M4 operate under the demagnetization current, all of their stator NdFeB magnets have a risk of partial irreversible demagnetization. However, the area of irreversible demagnetization is small and it is deemed acceptable.

4.5 Loss and Efficiency Analysis

Fig. 15 shows the loss characteristics of the four machines. It can be noticed that at different speeds, the PM loss of M2 is maximum due to larger leakage flux between the stator poles, while the iron loss of M3 is maximum due to longer flux path. Due to the utilization of abundant working harmonics, the PM loss of M4 is higher than that of M3. Moreover, the iron loss and PM loss of M1 are minimal due to its low frequency and low consumption of PMs. Based on this, the losses and efficiency of the four machines at the rated load and speed are listed in Table 7. Fig. 16 shows the efficiency characteristics of the four machines. The efficiency of M4 is higher than that of other machines due to its higher torque capability and lower losses.

4.6 Overhang Structure Analysis

The leakage flux of CP PM machine at both ends is generated due to the end effect, which reduces its torque capacity. Therefore, to further improve the torque and internal space utilization, an overhang structure is adopted to maximize the use of the internal space. Fig. 17 shows the overhang structure, i.e., extending only the length of rotor ferrites. Based on 3D FEM, the effect of overhang length on torque of the four machines is investigated, as shown in Fig. 18. It can be noticed that the additional flux path shown in Fig. 18(a) is present at the end of CP PM machine with overhang structure, which would enhance the effective air-gap flux to improve torque. Moreover, the torque of the four machines increases and then flattens with the increase of ferrite overhang length, as shown in Fig. 18(b). This is because the effective air-gap flux increases only when k_{ro} is more than a certain length. As a result, a suitable overhang length needs to be chosen to balance the relationship between torque and cost. The torque values for M1, M2, M3, and M4 are 5 Nm, 4.4 Nm, 8.6 Nm, and 9.71 Nm, corresponding to k_{ro} values of 1.24, 1.28, 1.32, and 1.2, respectively. Compared to the machines without the overhang structure, the torques are improved by 6.06%, 13.99%, 4.67%, and 3.31%, respectively. The results indicate that the overhang structure has the greatest impact on the torque of M2.

Table 7. Loss and efficiency of four machines

	M1	M2	M3	M4
Rated speed (r/min)			300	
Copper loss (W)			51	
Iron loss (W)	3.31	3.82	9.99	5.61
PM eddy current loss (W)	0.08	0.26	0.13	0.15
Output power (W)	174.54	131.31	273.61	337.7
Efficiency (%)	76.24	70.45	81.74	85.61

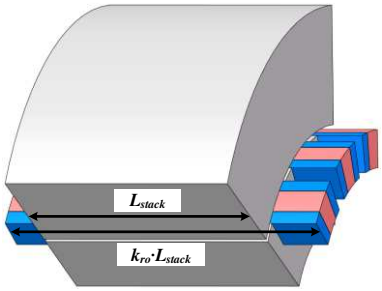

Fig. 17. Rotor overhang parameters.

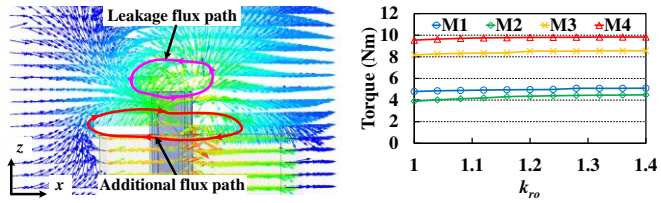

(a) (b)

Fig. 18. (a) Magnet field distribution. (b) Torque versus k_{ro} at rated current.

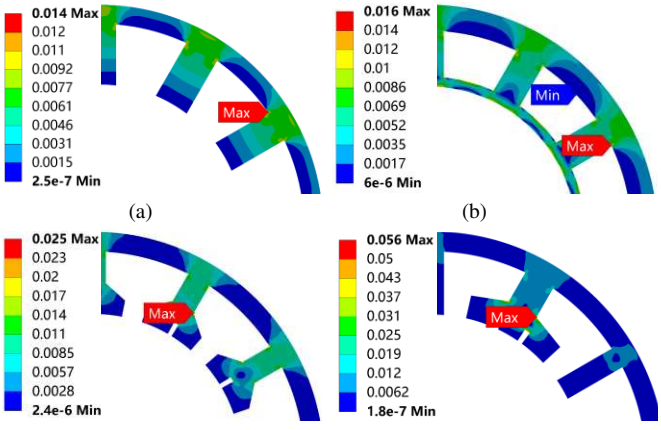

(a) (b) (c) (d)

Fig. 19. Equivalent stress distribution. (a) M1. (b) M2. (c) M3. (d) M4.

4.7 Equivalent Stress Analysis

To compare the stator mechanical robustness of the machine, the equivalent stress analysis can be performed in the ANSYS Workbench [25]. The stator equivalent stress distribution of the four machines at the rated speed of 300 r/min is shown in Fig. 19. It can be seen that the maximum stresses of M1, M2, M3, and M4 are 0.014 MPa, 0.016 MPa, 0.025 MPa, and 0.056 MPa, respectively, which are far less than the ultimate tensile strength of the material (420 MPa). Thus, the proposed machine does not suffer from strong stress.

5. Experimental Verifications

To verify the effectiveness of the proposed split stator-pole HDPM machine, a 12s/34p prototype with k_{ro}=1.2 was manufactured based on the specifications provided in Table 1, Fig. 2(d), and Fig. 17. The prototype assemblies are shown in Fig. 20, where the rotor was wound with non-woven cloth to prevent the rotor ferrites from falling off, and the test rig is shown in Fig. 21. The servo motor, torque sensor, and prototype were connected via couplings, with an OMRON E6B2-CWZ6C digital incremental encoder installed between the torque sensor and the prototype to capture rotor position. The servo machine, which acted as the prime mover, drove the prototype for no-load testing. Furthermore, the prototype was powered by a voltage source inverter composed of two intelligent power modules PM100CVA120 and a DSP TMS320F28377 control board. The magnetic powder brake was utilized to apply load, and the resulting torque was measured by the torque sensor. The current waveforms were displayed on the Tektronix MDO3034 oscilloscope by Tek A622 current clamps. The efficiency was measured using a YOKOGAWA-WT5000 power analyzer.

Fig. 22 shows the comparison of measured and 3D FEM back-EMFs. The measured amplitudes of the fundamental back-EMF versus speed are consistent with 3D FEM results. The phase back-EMF waveforms at the rated speed of 300 r/min are sinusoidal and symmetrical, and the amplitudes of measured and simulated fundamental back-EMFs are 11.34 V and 11.84 V, respectively. The error between them is about 4.22%, which is mainly caused by mechanical processing errors but within the acceptable range.

The instantaneous torque at rated current was measured by adopting I_d = 0 A control strategy, as shown in Fig. 23, where the manufacturing tolerances and vibration disturbances reduced the measured torque compared to the 3D FEM results, with an error of 5.17%. Fig. 24(a) shows the measured and 3D FEM torque-current angle performances. It can be observed that the measured torque is slightly lower than the 3D FEM results due to fringing effects and manufacturing tolerances, but the difference remains within an acceptable range. Fig. 24(b) shows the comparison of measured and 3D FEM average torques versus peak current. The measured results exhibit good agreement with the 3D FEM results, with a maximum error of 7.9%. This discrepancy is attributed to the aforementioned errors. Furthermore, the machine efficiency was measured by power analyzer, and the efficiency versus speed at rated peak current is shown in Fig. 25. The measured efficiency is slightly lower than that of 3D FEM due to the relative error of the core loss in the 3D FEM model and the influence of mechanical loss. However, the variation trend of the measured efficiency is consistent with that of 3D FEM. Hence, the results can validate the effectiveness of the proposed machine.

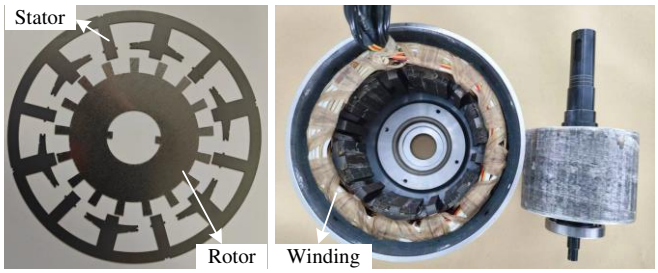

Fig. 20. Prototype. (a) Stator-rotor lamination. (b) Stator and rotor.

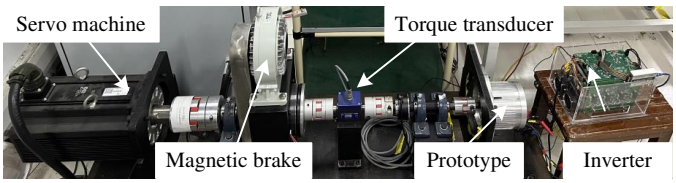

Fig. 21. Experimental platform.

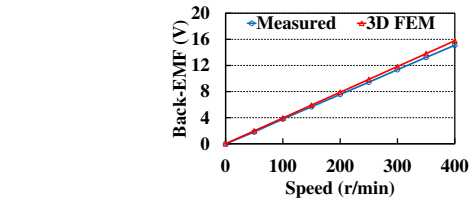

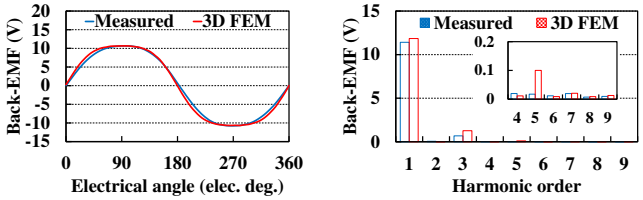

Fig. 22. Comparison of measured and predicted back-EMFs. (a) Fundamental amplitude versus speed. (b) Waveforms. (c) Spectra.

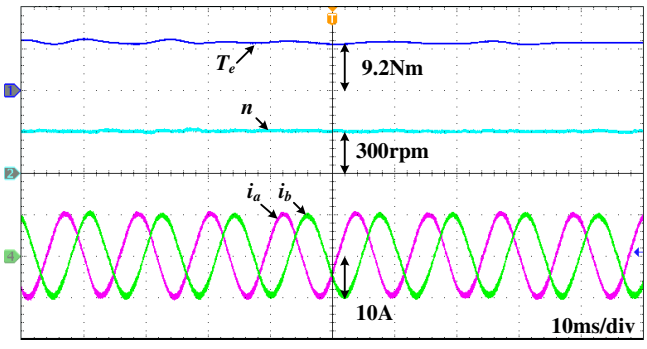

Fig. 23. Instantaneous torque at rated load.

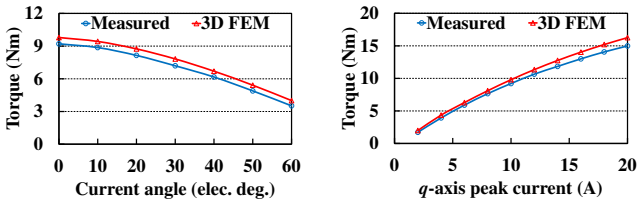

(a) (b)

Fig. 24. Comparison of measured and predicted (a) torque versus current angle and (b) torque versus *q*-axis peak current.

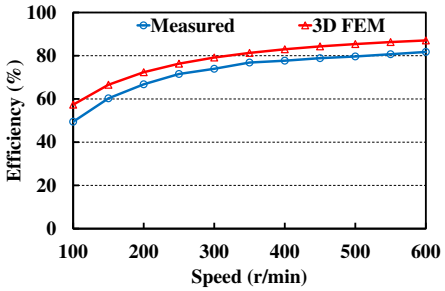

Fig. 25. Comparison of measured and predicted efficiency versus speed

6. Conclusion

This paper analyzed and compared the working harmonics and electromagnetic performances of the four HDPM machines with different ASP topologies, which were optimized by NSGA-II. The hybrid magnetic pole design consisting of stator NdFeB magnets and rotor Halbach-array ferrites are combined with the CP array to increase PM utilization and reduce rare-earth material usage. This combination provides a material selection basis for cost-sensitive HDPM machine design. The results demonstrate that the machines can generate abundant harmonics due to the ASP design and bidirectional flux modulation effect. Specifically, the major working harmonics adjusted by the ASP design are involved in torque production. Compared to the stator-pole HDPM machine with similar PM usage and the same copper loss, the proposed split stator-pole HDPM machine exhibits a significant improvement in torque of approximately 23.4%, which indicates that the proposed machine generates more effective working harmonics. Furthermore, the mechanism of rotor-ferrite overhang structure to improve torque and their length effect on torque were also investigated by 3D FEM. The performance enhancement induced by the overhang structure demonstrates that the torque density of the HDPM machine can be further optimized through selecting the appropriate length when the internal axial space of the machine permits. Compared with other machines studied, the proposed machine can offer better overall performance such as higher torque density and efficiency. Finally, a prototype of the proposed machine was fabricated and experimentally tested to validate its effectiveness.

Acknowledgements

This work was supported in part by the National Natural Science Foundation of China (Project No. 52277052).

Declarations

Conflict of interest All authors certify that they have no affiliations with or involvement in any organization or entity with any financial interest or non-financial interest in the subject matter or materials discussed in this manuscript.

References

1. J. Wang, W. Geng, J. Guo, L. Li, and Z. Zhang, "Design and performance comparison of novel flux-concentrating IPM machines for power generation system application of extended-range electric vehicle," *IEEE Trans. Ind. Electron.*, vol.70, no.5, pp.4450-4460, May 2023.
2. S. Han and C. Ahn, "Optimal preemptive controller enabling electric driving of a hybrid electric vehicle in a zero emission zone," *IEEE Trans. Veh. Technol.*, vol.73, no.4, pp.4729-4741, Apr. 2024.
3. H. Zhou, W. Tao, G. Jiang, G. -J. Li, and G. Liu, "Reduction of saturation and unipolar leakage flux in consequent-pole PMV machine," *IEEE J. Emerg. Sel. Topics Power Electron.*, vol.10, no.2, pp.1870-1880, Apr. 2022.
4. H. Yang, Z. Q. Zhu, H. Lin, H. Li, and S. Lyu, "Analysis of consequent-pole flux reversal permanent magnet machine with biased flux modulation theory," *IEEE Trans. Ind. Electron.*, vol.67, no.3, pp.2107-2121, Mar. 2020.
5. L. Fang, D. Li, X. Ren, and R. Qu, "A novel permanent magnet vernier machine with coding-shaped tooth," *IEEE Trans. Ind. Electron.*, vol.69, no.6, pp.6058-6068, Jun. 2022.
6. J. Wang, W. Geng, Q. Li, L. Li, and Z. Zhang, "A new flux-concentrating rotor of PM machine for electric vehicle application," *IEEE Trans. Ind. Electron.*, vol.69, no.11, pp.10882–10892, Nov. 2022.
7. H. Qu, Z. Q. Zhu, and H. Li, "Analysis of novel consequent pole flux reversal permanent magnet machines," *IEEE Trans. Ind. Appl.*, vol.57, no.1, pp.382-396, Jan.-Feb. 2021.
8. S. Cai, H. Chen, X. Yuan, Y. -C. Wang, J. -X. Shen and C. H. T. Lee, "Analysis of synergistic stator permanent magnet machine with the synergies of flux-switching and flux-reversal effects," *IEEE Trans. Ind. Electron.*, vol.69, no.12, pp.12237-12248, Dec. 2022.
9. Q. Lin, S. Niu, F. Cai, W. Fu and L. Shang, "Design and optimization of a novel dual-PM machine for electric vehicle applications," *IEEE Trans. Veh. Technol.*, vol.69, no.12, pp.14391-14400, Dec. 2020.
10. Y. Zheng, Y. Yin, M. Kang and Y. Fang, "Design and analysis of a novel dual-PM flux reversal machine for electric vehicle propulsion," *IEEE Trans. Transp. Electrific.*, vol.9, no.2, pp.2830-2838, Jun. 2023.
11. L. Xu, W. Zhao, M. Wu and J. Ji, "Investigation of slot–pole combination of dual-permanent-magnet-excited vernier machines by using air-gap field modulation theory," *IEEE Trans. Transp. Electrific.*, vol.5, no.4, pp.1360-1369, Dec. 2019.
12. L. Xu, W. Zhao, G. Liu, J. Ji and S. Niu, "A novel dual-permanent-magnet-excited machine with non-uniformly distributed permanent-magnets and flux modulation poles on the stator," *IEEE Trans. Veh. Technol.*, vol.69, no.7, pp. 7104-7115, Jul. 2020.
13. K. Yang, F. Zhao, Y. Wang, and Z. Bao, "Consequent-pole flux reversal permanent magnet machine with halbach array magnets in rotor slot," *IEEE Trans. Magn.*, vol.57, no.2, pp.1-5, Feb. 2021.
14. C. Gong and F. Deng, "Design and optimization of a high-torque-density low-torque-ripple vernier machine using ferrite magnets for direct-drive applications," *IEEE Trans. Ind. Electron.*, vol.69, no.6, pp.5421-5431, Jun. 2022.

15. W. Zhao, Q. Hu, J. Ji, Z. Ling and Z. Li, "Torque generation mechanism of dual-permanent-magnet-excited vernier machine by air-gap field modulation theory," *IEEE Trans. Ind. Electron.*, vol.70, no.10, pp.9799-9810, Oct. 2023.
16. H. Xu, Z. Q. Zhu, Y. Zhou and L. Chen, "Contributions of stator and rotor PMs in dual-PM machines with different stator and rotor pole number combinations," *IEEE Trans. Energy Convers.*, vol.39, no.1, pp.516-532, Mar. 2024.
17. Y. Gao, M. Doppelbauer, R. Qu, D. Li and H. Ding, "Synthesis of a flux modulation machine with permanent magnets on both stator and rotor," *IEEE Trans. Ind. Appl.*, vol.57, no.1, pp.294-305, Jan.-Feb. 2021.
18. X. Zhu, S. Li, S. Zheng, L. Quan, D. Fan and X. Zeng, "Torque component redistribution and enhancement for hybrid permanent magnet motor with permanent magnet offset placement," *IEEE Trans. Transp. Electrific.*, vol.9, no.1, pp.631-641, Mar. 2023.
19. S. Kazemisangdehi, Z. Q. Zhu, Y. Zhou, H. Liu, L. Chen and L. Yang, "Novel parallel hybrid rare-earth and ferrite magnets in V-spoke interior PM synchronous machine," *IEEE Trans. Ind. Appl.*, doi: 10.1109/TIA.2024.3524978.
20. Q. Wang, S. Niu, and L. Yang, "Design optimization and comparative study of novel dual-PM excited machines," *IEEE Trans. Ind. Electron.*, vol.64, no.12, pp.9924–9933, Dec. 2017.
21. B. Zang and Y. Chen, "Multiobjective optimization and multiphysics design of a 5 MW high-speed IPMSM used in FESS based on NSGA-II," *IEEE Trans. Energy Convers.*, vol.38, no.2, pp.813-824, Jun. 2023.
22. Y. Hua, H. Zhu, M. Gao, and Z. Ji, "Multiobjective optimization design of permanent magnet assisted bearingless synchronous reluctance motor using NSGA-II," *IEEE Trans. Ind. Electron.*, vol.68, no.11, pp.10477-10487, Nov. 2021.
23. Z. Li, X. Huang, A. Liu, Z. Chen, Y. Yu and L. Wu, "Analytical calculation of eccentric surface-mounted permanent-magnet motor accounting for iron saturation," *IEEE Trans. Transp. Electrific.*, vol.8, no.3, pp.3441-3450, Sept. 2022.
24. H. Yang, H. Lin, Z. Q. Zhu, S. Lyu, and Y. Liu, "Design and analysis of novel asymmetric-stator-pole flux reversal PM machine," *IEEE Trans. Ind. Electron.*, vol.67, no.1, pp.101-114, Jan. 2020.
25. J. Cheng, W. Zhang, X. Yin, F. Ding, "Multi-objective optimization and analysis of divided-layer varying-network magnetic circuit based axial field flux-switching magnetic gear composite motors," *J. Power Electron.*, doi:10.1007/s43236-024-00900-7.

Guangyao Jiang received the B.Sc. degree in electrical engineering from Anhui Polytechnic University, Wuhu, China, in 2018, and the M.Sc. degree in electrical engineering at Jiangsu University, Zhenjiang, China, 2022. He is currently working toward the PH.D. degree in electrical engineering at Jiangsu University, Zhenjiang, China.

His current research interests include PM machine design and optimization.

Huawei Zhou (M'16–SM'25) received the B.Sc. and M.Sc. degrees in control engineering from Jiangsu University, Zhenjiang, China, in 2003 and 2006, respectively, and the Ph.D. degree in electrical engineering from the Graduate University of Chinese Academy of Sciences, Beijing, China, in 2012.

He has been with Jiangsu University since 2003, where he is currently a Professor in the School of Electrical and Information Engineering. From 2017 to 2018, he was a visiting academic with the Department of Electronic and Electrical Engineering, University of Sheffield, Sheffield, U.K. His teaching and research interests include electric machines design, PM motor drive, fault-tolerance analysis, and intelligent control.

Chen Ye received the B.Sc. degree in electrical and electronic engineering from the Jincheng College, Nanjing University of Aeronautics and Astronautics, Nanjing, China, in 2019, and the M.Sc. degree in electrical engineering from Jiangsu University, Zhenjiang, China, 2022, where he is currently pursuing the Ph.D. degree in electrical engineering.

His current research interests include drive and control of PM motors.

Guang-Jin Li (M'10–SM'16) received the bachelor's degree from Wuhan University, China, in 2007, the master's degree from the University of Paris XI, France, in 2008, and the PhD degree from the Ecole Normale Supérieure (ENS) de Cachan, Paris, France, in 2011, all in electrical and electronic engineering.

He joined the Electrical Machines and Drives (EMD) Group, University of Sheffield, Sheffield, U.K., in June 2012, as a Postdoctoral Research Associate, where he was appointed as an Assistant Professor, in September 2013, and promoted to Associate Professor in January 2018 and Professor in January 2022. His main research interests include the design, fault diagnostics, and thermal management of electrical machines for renewable energy, automotive, and electrical aircrafts.

Yu Zeng (M'22) received the B.Sc. and M.Sc. degrees in electrical engineering from Jiangsu University, Zhenjiang, China, in 2014 and 2017, respectively, and the Ph.D. degree from the Department of Electrical Engineering, Southeast University, Nanjing, China, in 2021.

Since 2022, he has been with Jiangsu University, where he is currently a Lecture with the School of Electrical and Information Engineering. His research interests include the design and analysis of permanent magnet synchronous machines and brushless doubly-fed machines.